Low-frequency excitations of a disordered Wigner crystal

Ulrich Wulf
Technische Universität Cottbus, Fakultät 1, Postfach 101344, D-03013 Cottbus, Germany
(Received 8 September 1998)

We develop a consistent theory for the response of the disordered electron crystal in a strong magnetic field. The Coulomb interaction is taken in the Hartree-Fock approximation and the impurity interaction in the self-consistent Born approximation. We find two distinct phases, a crystalline phase at low disorder and an amorphous phase at stronger disorder. As in recent experiments by C.-C. Li, L. W. Engel, D. Shahar, D. C. Tsui, and M. Shayegan [Phys. Rev. Lett. **79**, 1353 (1997)] and by L. W. Engel, C.-C. Li, D. Shahar, D. C. Tsui, and M. Shayegan [Solid State Commun. **104**, 167 (1997)], we find in the crystalline phase a well-defined excitation peak which we identify as a magnetophonon in the disordered system. In the experiments at lower magnetic fields a strong damping of the excitation is found and finally the mode disappears still in the insulating regime. Based on our calculations we suggest a Landau damping picture as an explanation: At lower magnetic field a transition to the amorphous phase takes place and the energy gap of the crystalline phase vanishes. In consequence the magnetophonon can couple to single-particle transitions which leads to Landau damping of this mode. [S0163-1829(99)09509-0]

I. INTRODUCTION

The crystallization of a low-density electron gas at low temperatures was predicted by Wigner[1] a long time ago. Up to now experimental evidence for such an electron solid has been found in two-dimensional electron gases on the surface of liquid helium and in semiconductor heterostructures. In general, in semiconductor systems the application of a strong magnetic field is necessary for the solidification because, first, the small electronic band mass leads to enhanced quantum fluctuations, second, the relatively large dielectric constant weakens the Coulomb interaction, and, third, the relatively large electron density causes an enhanced kinetic energy in the uncondensed state. Experimental evidence for an electron solid at zero magnetic field are rare.[2] In agreement with experiments (Refs. 3–6) and Refs. 7,8, calculations of the ground-state energy show that without disorder the crystal is expected to form in the strong magnetic field at filling factors between $\nu=1/5$ and $\nu=1/7$ in the electron system[9] and in the hole crystal around $\nu=1/3$.[10] Since the energy of the fractional quantum Hall liquid is at $\nu=1/5$ only slightly smaller than in the electron crystal, a reentrant metal-insulator transition at this filling factor as a termination of the quantum Hall regime is experimentally observed. The interpretation in terms of the formation of a Wigner crystal in these systems has been supported by measurements of the thermally activated dc transport,[4,5] the threshold behavior of the nonlinear conductance,[11,5,12] and the detection of increased noise for greater voltages than the threshold voltage.[5,12] Furthermore, in ac measurements in the GHz regime a resonance was observed that has been interpreted as pinning mode[6] of the Wigner crystal or directly as its magnetophonon mode with the expected dispersion $\propto q^{2/3}$.[13,14]

The important role of disorder has been demonstrated in more recent experiments on lower mobility electron[15–17] or hole systems.[18] Here the metal-insulator transition occurs at larger filling factors, up to $\nu\sim 0.6$ in electron systems.[15] While in low disorder samples one sees a reentrant fractional quantum Hall effect at filling factors as low as $\nu=1/5$ and (weaker) $\nu=2/9$ at stronger disorder only the $\nu=1$ and the 1/3 fraction is observed. In this regime there are a number of other experimental features that cannot be accounted for in the picture of a simple pinned Wigner crystal phase: A universal conductance at the metal-insulator transition,[15] a much weaker than exponential (algebraic) dependence of ρ_{xx} on $1/T$,[8,5] and the damping (finally overdamping) of the pinning mode in weaker magnetic fields associated with a decrease of its frequency.[18,16] Alternative models for systems with stronger disorder have been discussed; single-particle localization,[3,17] the formation of a Hall insulator,[19,15,8] and the existence of a glassy (amorphous) Wigner phase.[20,21,5]

In this paper we develop a mean-field theory for the disordered Wigner crystal in which the competition between the Coulomb interaction and disorder can be calculated microscopically and determine consistently its ac and dc response properties: To this end we follow the approach of Ando who takes into account the impurity interaction in the noninteracting system in the self-consistent Born approximation[22] and add to this model the Coulomb interaction in the Hartree-Fock approximation. From Ref. 23 it directly follows how the response properties have to be evaluated to preserve the basic conservation laws. Our results support the idea of the formation of a glassy state at high disorder: While for weak disorder we find a crystalline phase with a typical pronounced energy gap at the Fermi level for strong disorder a state with a more or less pronounced dip of the density of states at the Fermi level results. In this state the hexagonal modulation of the electron density is reduced but stays finite. The finite hexagonal order in our mean-field theory and the tails of the density of states in the energy gap leading to a finite density of states at the Fermi level, we interpret as signatures of a very short-range order in an amorphous or glassy phase.

In a previous paper[24] we showed that we can explain in this picture the experimentally measured turnover from an exponential dependence of the resistance vs $1/k_BT$ to be expected in the electron solid to a much softer (algebraic) dependence in the amorphous state. Here we want to describe our approach in detail and compare our results to the ac measurements of Refs. 18,16 mentioned earlier in this introduction: In a strong magnetic field a sharp resonance in the GHz regime is found which becomes increasingly damped at weaker magnetic fields and finally vanishes while still in the insulating regime. In our model we offer an interpretation of this phenomenon as a Landau damping effect: At first we establish that the transition between crystalline phase and the amorphous phase can be driven by a decreasing magnetic field, i.e., the energy gap is reduced to zero. Therefore, at strong magnetic fields, in the crystalline phase, the frequency of the resonance is well in the energy gap of the electron crystal. At smaller magnetic fields the energy gap becomes smaller and the pinning mode couples to single-particle transitions (Landau damping). At yet smaller magnetic fields the energy gap vanishes and the amorphous phase sets in where the pinning mode vanishes because of overdamping.

II. FORMALISM

A. The ground state

For the major interactions in the system, the Coulomb interaction and the disorder potential, we take the Hartree-Fock approximation (HF) and the the self-consistent Born approximation (SCBA). These approximations are discussed and justified in Refs. 25,26. For the sake of completeness and readability we give a summary of the corresponding formalism in this subsection: In the finite-temperature Matsubara formalism we write for the self-energy

$$\Sigma(\vec{r},\vec{r}\,',\omega_n)=G(\vec{r},\vec{r}\,',\omega_n)\langle V_{\rm dis}(\vec{r})V_{\rm dis}(\vec{r}\,')\rangle + \delta(\vec{r}-\vec{r}\,')\int d\vec{r}\,''n(\vec{r}\,'')\frac{e^2}{|\vec{r}\,''-\vec{r}\,'|} - \frac{e^2}{|\vec{r}-\vec{r}\,'|}\frac{1}{\beta}\sum_{\omega_n'}\lim_{\eta\to 0+}\exp(i\omega_n'\eta)G(\vec{r},\vec{r}\,',\omega_n'). \tag{1}$$

Here $\langle\ \rangle$ is the disorder average of the correlation function of the disorder potential $V_{\rm dis}(\vec{r})$, $\omega_n=(2n+1)\pi/(\beta\hbar)$ are the fermionic Matsubara frequencies, and $\beta=1/(k_BT)$. With this self-energy we solve Dyson's equation

$$G(\vec{r},\vec{r}\,',\omega_n)=G_0(\vec{r},\vec{r}\,',\omega_n)+\int d\vec{r}\,''d\vec{r}\,'''G_0(\vec{r},\vec{r}\,'',\omega_n)\times\Sigma(\vec{r}\,'',\vec{r}\,''',\omega_n)G(\vec{r}\,''',\vec{r}\,',\omega_n). \tag{2}$$

A considerable simplification for the solution of Dyson's equation (Fig. 1) is achieved using a representation $G(\vec{k},z)$ of the Green's function

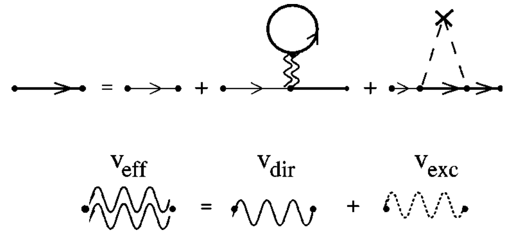

FIG. 1. Dyson's equation for the ground state in our approximation: Impurity interaction in dashed lines with crosses and effective Coulomb interaction in double wavy line.

$$G(\vec{r},\vec{r}\,',z)=\sum_{X,X'}G(X,X',z)\Phi_X(\vec{r})\Phi^*_{X'}(\vec{r}\,') =\sum_{\vec{k}X}G(\vec{k},z)\exp\left(ik_xX-i\frac{k_xk_yl^2}{2}\right)\times\Phi_X(\vec{r})\Phi^*_{(X-k_yl^2)}(\vec{r}\,'), \tag{3}$$

where $G(\vec{k},z)$ depends on only one vector $\vec{k}$ of the hexagonal reciprocal lattice. The $\Phi_X(\vec{r})$ are the lowest Landau-level eigenfunctions

$$\Phi_X(\vec{r})=\frac{1}{\sqrt{\sqrt{\pi}lL_y}}\exp\left[i\frac{Xy}{l^2}\right]\exp\left[-\frac{(x-X)^2}{2l^2}\right], \tag{4}$$

of the problem without Coulomb and disorder interaction in the Landau gauge with the eigenenergy $\epsilon_0=\hbar\omega_c/2$. These functions depend on the center coordinate X. The cylcotron resonance frequency is ω_c and l is the magnetic length. In our representation Eq. (3) we only take into account the lowest Landau level, which is justified in strong magnetic fields.

As derived in Ref. 26 we find

$$G(\vec{k},z)=G^0(\vec{k},z)+G^0(z)\sum_{\vec{p}}\Sigma(\vec{k}-\vec{p},z)G(\vec{p},z)\times\cos\left[\frac{l^2}{2}(\vec{k}\times\vec{p})_z\right], \tag{5}$$

where $\vec{p}$ is a vector of the reciprocal lattice and the unperturbed Green's function G^0 is given by

$$G^0(\vec{k},z)=\delta_{\vec{k},0}\frac{1}{i\hbar\omega_n-(\epsilon_0-\mu)}. \tag{6}$$

For the self-energy we obtain $\Sigma(\vec{k},z)=\Sigma(\vec{k},z)^{\rm dis}+\Sigma(\vec{k},z)^{\rm HF}$ with

$$\Sigma^{\rm dis}(\vec{k},z)=\frac{1}{4}G(\vec{k},z)\Gamma^2(\vec{k}) \tag{7}$$

and

$$\Gamma^2(\vec{k})=\Gamma^2\exp\left(-\frac{y^2}{2}\right), \tag{8}$$

where $y=|\vec{k}|l$, $\Gamma^2=4n_I V_0^2/2\pi l^2$, and n_I is the number of δ scatterers per area with individual scattering potentials $V(\vec{r})=V_0\delta(\vec{r})$. For the self-energy of the Hartree-Fock term it follows that

$$\Sigma(\vec{k},z)^{\mathrm{HF}}=W_0(\vec{k})\rho(\vec{k}) \tag{9}$$

with

$$W_0(\vec{k})=\frac{e^2}{l}\exp\left(-\frac{y^2}{2}\right)\left[\frac{1}{y}(1-\delta_{\vec{k},0}) - \exp\left(\frac{y^2}{4}\right)\left(\frac{\pi}{2}\right)^{1/2} I_0\left(\frac{y^2}{4}\right)\right], \tag{10}$$

where I_0 is the modified Bessel function of the first kind. Furthermore,

$$\rho(\vec{k})=-\frac{1}{\pi}\int_{-\epsilon}^{\epsilon} d\epsilon\, n_F(\epsilon)\mathrm{Im}[G(-\vec{k},\epsilon-\mu+i\eta)], \tag{11}$$

with the Fermi distribution function $n_F(\epsilon)=(\exp[(\epsilon-\mu)\beta]+1)^{-1}$.

The self-energy $\Sigma(\vec{k},z)^{\mathrm{HF}}$ in Eq. (9) is formally equivalent to a self-energy term resulting in a Hartree approximation with an effective Coulomb propagator[27]

$$V_{\mathrm{eff}}(\vec{k})=\frac{2\pi e^2}{|k|}\left[(1-\delta_{\vec{k},0})-\exp\left(\frac{y^2}{4}\right)y\left(\frac{\pi}{2}\right)^{1/2} I_0\left(\frac{y^2}{4}\right)\right]. \tag{12}$$

To show this we start from a general single-particle potential of the form

$$V(\vec{r})=\sum V(\vec{k})\exp(i\vec{k}\vec{r}). \tag{13}$$

As derived in Ref. 25 the self-energy Σ_{pot} that results in Eq. (5) from this potential is given by

$$\Sigma_{\mathrm{pot}}(\vec{k})=\exp\left(-\frac{y^2}{4}\right)V(\vec{k}). \tag{14}$$

Equating $\Sigma(\vec{k},z)^{\mathrm{HF}}$ and Σ_{pot} and making use of the identity

$$n(\vec{k})=\frac{1}{2\pi l^2}\exp\left(\frac{-y^2}{4}\right)\rho(-\vec{k}) \tag{15}$$

derived in Ref. 26 [$n(\vec{k})=n(-\vec{k})$ is the Fourier transform of the electron density n], we find

$$V(\vec{k})=n(\vec{k})\frac{2\pi e^2}{|k|}\left[(1-\delta_{\vec{k},0})-\exp\left(\frac{y^2}{4}\right)y\left(\frac{\pi}{2}\right)^{1/2} I_0\left(\frac{y^2}{4}\right)\right]. \tag{16}$$

This is the single-particle potential obtained in the Hartree approximation with an effective Coulomb propagator given by Eq. (12). The first factor in V_{eff} is the usual direct term where the interaction with a positive background is removed for $\vec{k}=0$. The second term arises from the Fock diagram of the self-energy and leads to a modification of the Coulomb propagator. Using the effective Coulomb propagator we can write a simplified Dyson's equation for the ground state as shown diagrammatically in Fig. 1. The Hartree-like diagram for the combined Hartree-Fock interaction is the second diagram on the right-hand side of the first line in Fig. 1. The third term is the diagrammatic representation of the self-energy of the impurity interaction.

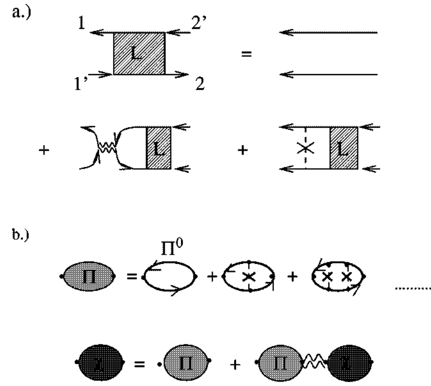

FIG. 2. (a) Eqs. (19)–(21) in diagrammatic form. (b) Alternative way of generating exactly the same diagrams, where 1 and 1' and 2 and 2' are closed.

B. The dynamic response

Our analysis of the dynamic response properties starts with the susceptibility χ. We adopt the formalism and notation in Ref. 23 and define

$$\chi(1,2)=\frac{\delta\langle n(1)\rangle_c}{\delta U(2)}=-i\frac{\delta G(1,1^+)_c}{\delta U(2)}. \tag{17}$$

Here 1 stands for the quadruple $(\vec{r}_1,t_1)$ and $U(2)$ is an external potential perturbation contributing to the Hamiltonian density $U(\vec{r}_2,t_2)n(\vec{r}_2,t_2)$, where n is the electronic particle density. The index c denotes the causal response and $\langle\ \rangle$ the thermal expectation value. According to Ref. 23 we write

$$\left.\frac{\delta G(1,1^+;U)}{\delta U(2)}\right|_{U=0}=L(12,1^+2^+), \tag{18}$$

where $G(1,1';U)$ is the U-dependent thermal Matsubara Green's function which depends on a complex time argument. As is carried out in Sec. III F for the present case the causal Green's function can be obtained from the Matsubara Green's function by replacing the complex frequency $i\omega$ by $\omega+i\delta$. This procedure is discussed in detail in Ref. 28. Following Ref. 23 we can write for L an integral equation

$$L(12,1'2')=-G(1,2')G(2,1')+\int d3\,d4\,d5\,d6\,G(1,3) \times G(4,1')\Xi(35,46)L(62,52), \tag{19}$$

where $G(1,2')=G(1,2',U=0)$ and

$$\Xi(35,46)=\left[\frac{\delta\Sigma(3,4)}{\delta G(6,5)}\right]_{U=0}. \tag{20}$$

In Fig. 2(a) we write Eq. (19) in diagrammatic form with a self-energy given by

$$[\Sigma(3,4)]_{U=0} = -i\delta(3-4)\int d2 v_{\rm eff}(\vec r_3-\vec r_2)\delta(t_3-t_2)G(2,2^+) + i\langle V_{\rm dis}(\vec r_3)V_{\rm dis}(\vec r_4)\rangle G(3,4). \tag{21}$$

It is obvious that exactly the same diagrams that are generated from the integral equations (18)–(21) in Fig. 2(a) can also be generated by a procedure demonstrated in Fig. 2(b): First, the ''ladder sum'' over all impurity interaction lines is carried out (see upper line). For a noninteracting homogeneous electron gas this summation has been carried out in Ref. 29. The corresponding ladder summation in the here considered interacting system with hexagonal density modulation reduces to the results in Ref. 29 in the case $\vec k=\vec k' =0$ (see Secs. C, D, and E). In the second step, a ''bubble summation'' over the effective Coulomb interaction follows (lower line). According to Eq. (18) the diagram for L has to be closed on the left and on the right side.

C. The bare bubble

We begin the evaluation of the ''ladder sum'' in Fig. 2(b), upper line, with the evaluation of the ''bare bubble'' Π^0 for which we write

$$\Pi^0(\vec r,\vec r\,',i\omega_n)=\frac{1}{\beta}\sum_{n'} G(\vec r,\vec r\,',i\omega_{n'}+i\omega_n)G(\vec r\,',\vec r,i\omega_{n'}). \tag{22}$$

In this expression our representation of the Green's function Eq. (3) is inserted. We introduce a two-dimensional Fourier transform to obtain

$$\begin{aligned}\Pi^0(\vec Q,\vec Q',i\omega_n) &= \int d\vec r\, d\vec r\,' \exp(-i\vec Q\vec r+i\vec Q'\vec r\,')\Pi^0(\vec r,\vec r\,',i\omega_n)\\ &= \sum_{n',X,X',k,k'} G(\vec k,i\omega_{n'}+i\omega_n)G(\vec k',i\omega_n)\\ &\quad\times\exp(ik_xX-ik_xk_yl^2/2+ik_x'X'-ik_x'k_y'l^2/2)\\ &\quad\times\langle X'-k_y'l^2|\exp(-i\vec Q\vec r)|X\rangle\\ &\quad\times\langle X-k_yl^2|\exp(i\vec Q'\vec r)|X'\rangle. \end{aligned}\tag{23}$$

Here

$$\langle X|\exp(i\vec Q\vec r)|X'\rangle=\exp[iQ_x(X+X')/2]\exp\times[-Q^2l^2/4]\delta_{X',X+Q_yl^2} \tag{24}$$

is the matrix element of the harmonic potential between the lowest Landau-level eigenstates with center coordinates X and X' given in Eq. (4). Because of the the periodicity of the system $\Pi^0(\vec Q,\vec Q',i\omega_n)$ is nonzero only if we can write $\vec Q =\vec q+\vec k$ and $\vec Q'=\vec q+\vec k'$, where $\vec q$ is an element of the first Brillouin zone of the reciprocal lattice and $\vec k$, $\vec k'$ are reciprocal-lattice vectors. Straightforward calculation yields for $\Pi^0(\vec q+\vec k,\vec q+\vec k',i\omega_n)\equiv\hat\Pi^0_{\vec k,\vec k'}(\vec q,i\omega_n)$

$$\hat\Pi^0_{\vec k,\vec k'}(\vec q,i\omega_n)=\frac{\hat A_{\vec k,\vec k'}(\vec q)}{\beta}\sum_{i\omega_n'}\hat\pi^0_{\vec k,\vec k'}(\vec q,i\omega_n,i\omega_n'), \tag{25}$$

with

$$\begin{aligned}\hat\pi^0_{\vec k,\vec k'}(\vec q,i\omega_n,i\omega_n') &= \sum_{\vec k''} G(\vec k''+\vec k,i\omega_n+i\omega_n')G(-\vec k''-\vec k',i\omega_n')\\ &\quad\times\exp\left[-\frac{il^2}{2}\vec q\times(\vec k+\vec k')\right]\exp\left[\frac{il^2}{2}\vec k''\times(2\vec q+\vec k+\vec k')\right], \end{aligned}\tag{26}$$

and

$$\hat A_{\vec k,\vec k'}(\vec q)=\frac{1}{2\pi l^2}\exp\left[-\frac{(\vec q+\vec k)^2l^2+(\vec q\,'+\vec k')^2l^2}{4}\right]. \tag{27}$$

D. Bubble with a single impurity interaction line

As an important intermediate step we analyze the bubble with a single impurity interaction line $\hat\Pi^1$ which is depicted in the second diagram of the right-hand side of the first line in Fig. 2(b) and given by

$$\begin{aligned}\Pi^1(\vec r_1,\vec r_2,i\omega_n)&=\frac{1}{\beta}\sum_{n'}\int d\vec r_3 d\vec r_4 G(\vec r_3,\vec r_2,i\omega_{n'}+i\omega_n)\\ &\quad\times G(\vec r_1,\vec r_3,i\omega_{n'}+i\omega_n)w(\vec r_3-\vec r_4)\\ &\quad\times G(\vec r_4,\vec r_1,i\omega_n)G(\vec r_2,\vec r_4,i\omega_n). \end{aligned}\tag{28}$$

Here w is the impurity interaction line

$$w(\vec r_1-\vec r_2)=\langle V_{\rm dis}(\vec r_1)V_{\rm dis}(\vec r_2)\rangle = \sum_\mu v^\mu(\vec r_1-\vec r_\mu)v^\mu(\vec r_2-\vec r_\mu), \tag{29}$$

where the $\vec r_\mu$ are the locations of the impurities that assumed to be evenly distributed in the x-y plane. Further, the impurities are taken to be identical with an individual scattering potential given by

$$v^\mu(\vec r)=\frac{V_0}{\pi d^2}\exp\left[-\frac{(\vec r-\vec r_\mu)^2}{d^2}\right], \tag{30}$$

where d parametrizes the range of the individual scattering potential and V_0 is its strength. We obtain for the Fourier transform of the impurity interaction line

$$w(q)=n_IV_0^2\exp\left[-\frac{(qd)^2}{2}\right], \tag{31}$$

where n_I is the density of the impurities which will be taken in the limit of δ scatterer $(d=0)$. As shown in Appendix A we obtain for the Fourier transform of Π^1 the same structure as for Π^0 in Eq. (25) (index 0 is replaced with index 1) with

$$\hat{\pi}^{1}_{\vec{k},\vec{k}'}(\vec{q},i\omega_n,i\omega_n') = \sum_{\vec{k}_1,\vec{k}_2} \hat{\pi}^{0}_{\vec{k},\vec{k}_1}(\vec{q},i\omega_n,i\omega_n')\hat{V}_{I;\vec{k}_1,\vec{k}_2}(\vec{q})\,\hat{\pi}^{0}_{\vec{k}_2,\vec{k}'}(\vec{q},i\omega_n,i\omega_n'), \tag{32}$$

or, in matrix notation

$$\hat{\pi}^1 = \hat{\pi}^0 \hat{V}_I \hat{\pi}^0. \tag{33}$$

Here we obtain

$$V_{I;\vec{k}_1,\vec{k}_2} = \delta_{\vec{k}_1,\vec{k}_2} \sum_{\vec{p}} \frac{w(p)}{S} \exp[il^2 \vec{p}\times(\vec{k}_1+\vec{q})] \exp\left[-\frac{(pl)^2}{2}\right], \tag{34}$$

where S is the area of the electron system. For δ scatterers we can find

$$V_{I;\vec{k}_1,\vec{k}_2}(\vec{q}) = \delta_{\vec{k}_1,\vec{k}_2} \frac{\Gamma^2}{4} \exp\left[-\frac{(\vec{q}+\vec{k}_1)^2 l^2}{2}\right], \tag{35}$$

where $\Gamma^2 = 4n_I V_0^2/2\pi l^2$ provides a measure of the disorder strength.

E. The ladder sum of the impurity vortex corrections

Using the procedure in Appendix A it is straightforward to show that a matrix structure analogous to Eqs. (32) and (33) results for each of the ladder diagrams of the impurity interaction [first equation of Fig. 2(b)]. For example, the second-order diagram yields in the matrix notation of Eq. (33)

$$\hat{\pi}^2 = \hat{\pi}^0 \hat{V}_I \hat{\pi}^0 \hat{V}_I \hat{\pi}^0. \tag{36}$$

The summation of the impurity ladder diagrams thus turns into a geometric series which can be carried out to give

$$\hat{\pi} = \sum_n \hat{\pi}^n = \hat{\pi}^0 [\hat{\delta} - \hat{V}_I \hat{\pi}^0]^{-1}, \tag{37}$$

with $(\hat{\delta})_{\vec{k}_1,\vec{k}_2} = \delta_{\vec{k}_1,\vec{k}_2}$. As in Eq. (25) we have

$$\hat{\Pi}_{\vec{k},\vec{k}'}(\vec{q},i\omega_n) = \frac{\hat{A}_{\vec{k},\vec{k}'}(\vec{q})}{\beta} \sum_{i\omega_n'} \hat{\pi}_{\vec{k},\vec{k}'}(\vec{q},i\omega_n,i\omega_n'). \tag{38}$$

F. Summation over the Matsubara frequencies

The Matsubara frequency summation in Eq. (38) can be carried out for each component of the matrix $\hat{\Pi}$. Using standard techniques[28,29] the sum over the complex Matsubara frequencies can be evaluated to give

$$\begin{aligned}\hat{\Pi}_{\vec{k},\vec{k}'}(\vec{q},\epsilon) = -\hat{A}_{\vec{k},\vec{k}'} \int_{-X}^{X} \frac{d\epsilon'}{2\pi i} n_F(\epsilon') [\hat{\pi}_{\vec{k},\vec{k}'}(\vec{q},\epsilon,\epsilon'+i\delta) \\ - \hat{\pi}_{\vec{k},\vec{k}'}(\vec{q},\epsilon,\epsilon'-i\delta) + \hat{\pi}_{\vec{k},\vec{k}'}(\vec{q},\epsilon,\epsilon'+\epsilon+i\delta) \\ - \hat{\pi}_{\vec{k},\vec{k}'}(\vec{q},\epsilon,\epsilon'-\epsilon-i\delta)],\end{aligned} \tag{39}$$

which is derived in Appendix B. The variables ϵ are on the real frequency axis where the imaginary part of the Green's function vanishes outside the energy interval $[-X,X]$.

For the calculation of $\hat{\Pi}(\vec{q},\epsilon)$ we start from the Green's function that is calculated along the real axis solving Dyson's equation [Eq. (5)] with contributions to the self-energy given by Eqs. (7) and (9). Using Eq. (26) we find $\hat{\pi}^0$ where products of Green's-function factors with different arguments enter. Then, according to Eq. (37) we obtain $\hat{\pi}$ which yields $\hat{\Pi}$ through Eq. (38). In the last step we perform the integration Eq. (39) along the real energy axis.

G. The dynamic Coulomb interaction

The calculation of the density-density response function χ is now carried out according to the second equation in Fig. 2(b) which is obviously equivalent to a geometric series. Using the matrix representation we obtain directly

$$\hat{\chi}(\vec{q},\epsilon) = \hat{\Pi}(\vec{q},\epsilon)[\hat{\delta} - \hat{V}^{\text{eff}}(\vec{q})\hat{\Pi}(\vec{q},\epsilon)]^{-1}, \tag{40}$$

with $\hat{V}^{\text{eff}}_{\vec{k},\vec{k}'}(\vec{q}) = \delta_{\vec{k},\vec{k}'} V_{\text{eff}}(\vec{q}+\vec{k})$ and

$$V_{\text{eff}}(\vec{q}) = \frac{2\pi e^2}{q}\left[1 - \left(\frac{\pi}{2}\right)^{1/2} ql \exp\left(\frac{q^2 l^2}{4}\right) I_0\left(\frac{q^2 l^2}{4}\right)\right]. \tag{41}$$

Equation (41) is identical with Eq. (12) except for the factor $\delta_{\vec{k},0}$ in the latter equation which is not necessary in Eq. (41) since we work at $q \neq 0$.

H. The response to the effective field

The correlation function χ evaluated in Eq. (40) describes the density response to the external potential, $\hat{\chi}_{\vec{k},\vec{k}'}(\vec{q},\omega) = \delta n(\vec{q}+\vec{k},\omega)/\delta v_{\text{ext}}(\vec{q}+\vec{k}',\omega)$. Through the continuity equation $\omega n(\vec{q},\omega) = \vec{q}\vec{j}(\vec{q},\omega)$ we can relate the density response to the induced currents. For each Fourier component $\vec{q}+\vec{k}$ we can write the continuity equation as

$$\begin{aligned}\omega\,\delta n(\vec{q}+\vec{k},\omega) &= -\frac{\vec{q}+\vec{k}}{e} \sum_{\vec{k}'} \hat{\sigma}_{\vec{k},\vec{k}'}(\vec{q},\omega)\,\delta\vec{E}(\vec{q}+\vec{k}',\omega) \\ &= \frac{-i}{e^2}(\vec{q}+\vec{k}) \sum_{\vec{k}'} \hat{\sigma}_{\vec{k},\vec{k}'}(\vec{q},\omega)(\vec{q}+\vec{k}') \\ &\quad \times \delta v_{\text{eff}}(\vec{q}+\vec{k}',\omega).\end{aligned} \tag{42}$$

In the first step we introduced the definition $\hat{\sigma}_{\mu,\nu;\vec{k},\vec{k}'}(\vec{q},\omega) = \delta J_\mu(\vec{q}+\vec{k},\omega)/\delta E_\nu(\vec{q}+\vec{k}',\omega)$, where μ and ν denote either x or y and $J = -ej$ is the electrical current density. Quantities in the linear-response regime are denoted by a δ. In the second step we neglect retardation to obtain purely longitudinal electric fields given by

$$\delta E(\vec{q}+\vec{k},\omega) = \frac{i}{e}(\vec{q}+\vec{k})\,\delta v_{\text{eff}}(\vec{q}+\vec{k},\omega). \tag{43}$$

Assuming a slowly varying external potential $\delta v_{\text{ext}}(\vec{r},t) = \delta v_0 \exp(i\vec{q}\vec{r})\exp(-i\omega t)$ with $\vec{q}\to 0$ we have to still expect short-range components $\delta v_{\rm eff}(\vec{q}+\vec{k},\omega)$, $\vec{k}\neq 0$ in the effective potential. However, a good approximation is obtained averaging out the short-range components in the effective potential in Eq. (42) (''*coarse graining method*'') in the long-range response. We then obtain

$$\omega\,\delta n(\vec{q},\omega)\approx\frac{-i}{e^2}\vec{q}\hat{\sigma}_{0,0}(\vec{q},\omega)\vec{q}\,\delta v_{\rm eff}(\vec{q},\omega). \tag{44}$$

We choose the x direction parallel to $\vec{q}$, i.e., in the direction of the electric field and define for the longitudinal conductivity

$$\sigma(\vec{q},\omega)\equiv\sigma_{x,x;0,0}(\vec{q},\omega)=\frac{i\omega e^2}{q^2}\frac{\delta n(\vec{q},\omega)}{\delta v_{\rm eff}(\vec{q}+\omega)}$$
$$=\frac{i\omega e^2}{q^2}\frac{\hat{\chi}_{0,0}(\vec{q},\omega)}{1+(2\pi e^2/q)\hat{\chi}_{0,0}(\vec{q},\omega)}. \tag{45}$$

In the last step we applied $\delta n(\vec{q},\omega)=\hat{\chi}_{0,0}(\vec{q},\omega)\,\delta v_0$ and $\delta v_{\rm eff}=\delta v_0+2\pi e^2\delta n/q$.

I. Power dissipation in an an external electric field and oscillator strengths

The power dissipation $P(\vec{q},\omega)$ in a periodically modulated two-dimensional electron system subjected to a longitudinal ac electric field has been considered in Ref. 31. Here we will review the results and adjust them to our case. We begin with the general expression[30]

$$P(\vec{q},\omega)=-\frac{e}{2}\int d^2r\,{\rm Re}[\vec{j}(\vec{r},\omega)\vec{E}(\vec{r},\omega)^*]$$
$$=-\frac{L_xL_ye}{2}\sum_{\vec{k}}{\rm Re}[\vec{j}(\vec{q}+\vec{k},\omega)\vec{E}(\vec{q}+\vec{k},\omega)^*], \tag{46}$$

where $\vec{j}$ is the particle current density, and $\vec{E}(\vec{r},\omega)^*$ is the complex conjugate of the total electric field which results as the response to a monochromatic external electric field $\vec{E}_{\rm ext}=\vec{E}_{\rm ext}(\vec{q},\omega)\,\exp(i\vec{q}\vec{r}-i\omega t)$. In the following we neglect retardation effects thus keeping only longitudinal fields $\vec{E}(\vec{q}+\vec{k},\omega)=E(\vec{q}+\vec{k},\omega)\vec{e}_{\vec{q}+\vec{k}}$. Therefore only longitudinal currents contribute to the dissipation. Using the equation of continuity we find

$$P(\vec{q},\omega)=-\frac{L_xL_y\omega e}{2}\sum_{\vec{k}}{\rm Re}\left[\frac{n(\vec{q}+\vec{k},\omega)}{|\vec{q}+\vec{k}|}E(\vec{q}+\vec{k},\omega)^*\right]. \tag{47}$$

We write in linear response for the induced electron density

$$\delta n(\vec{q}+\vec{k},\omega)=\hat{\chi}_{\vec{k},0}(\vec{q},\omega)\,\delta v_{\rm ext}(q,\omega)$$
$$=-\frac{ie}{q}\hat{\chi}_{\vec{k},0}(\vec{q},\omega)\,\delta E_{\rm ext}(q,\omega), \tag{48}$$

and for the effective field

$$\delta E(\vec{q}+\vec{k},\omega)=\delta_{\vec{k},0}\delta E_{\rm ext}(q,\omega)+i2\pi e\,\delta n(\vec{q}+\vec{k},\omega)$$
$$=[\delta_{\vec{k},0}+2\pi ie\hat{\chi}_{\vec{k},0}(\vec{q},\omega)]\,\delta E_{\rm ext}(q,\omega). \tag{49}$$

Inserting Eqs. (48) and (49) in Eq. (47) results in a power dissipation per area and unity of the external electric field

$$p_{\rm ext}(\vec{q},\omega)=\frac{P(\vec{q},\omega)}{L_xL_y|\vec{E}_{\rm ext}(\vec{q},\omega)|^2}=-\frac{e^2\omega}{2q^2}{\rm Im}\hat{\chi}_{0,0}(\vec{q},\omega)$$
$$=-\frac{\omega}{4\pi q}{\rm Im}\epsilon^{-1}_{0,0}(\vec{q},\omega). \tag{50}$$

From Eq. (46) it is, on the other hand, easy to derive the power dissipation per unity of the effective electric field

$$p(\vec{q},\omega)=\frac{P(\vec{q},\omega)}{L_xL_y|\vec{E}(\vec{q},\omega)|^2}=\frac{{\rm Re}[\sigma_{x,x;0,0}(\vec{q},\omega)]}{2}. \tag{51}$$

In analogy to Eq. (51) we define from Eq. (50)

$$\sigma^{\rm ext}_{x,x;0,0}(\vec{q},\omega)=i\frac{e^2\omega}{q^2}\hat{\chi}_{0,0}(\vec{q},\omega), \tag{52}$$

so that $p_{\rm ext}(\vec{q},\omega)={\rm Re}[\sigma^{\rm ext}_{x,x;0,0}(\vec{q},\omega)]/2$.

Equations (50) and (51) describe the power absorption in two different experimental circumstances. Equation (50) holds when the input power source provides the external electric field and Eq. (51) holds when the effective field is provided by the power source. The first case applies when there is basically no feedback between the Coulomb field of the induced charges in the electron system and the power source. The second case applies when these fields are transferred unweakened to the power source. A standard example for the second situation is the measurement of the dc conductivity of the two-dimensional electron gas with a contacted sample.

In the next section we will discuss rf experiments on the strong-magnetic-field insulating phase of a two-dimensional electron gas. These experiments are contactless, i.e., the voltage probes creating the electric field are spatially separated from the two-dimensional electron gas. As a typical example we discuss the experimental setup used in Ref. 13, which is described in more detail in Refs. 32 and 33. The conclusions are the same for the GHz measurements in Refs. 6, 18, and 16. In Ref. 13 the input power of a rf frequency source is transmitted via a meander line transducer into a detector. The meander line is located 300 nm above the plane of the two-dimensional electron gas. Through the meander structure a laterally modulated longitudinal electric field is generated in the plane of the two-dimensional electron gas and a small amount of the power sent to the meander line from the rf source is absorbed by the electrons.[33] If the longitudinal field is resonant with a mode of the electron system the dissipation increases and a dip in the transmitted power is observed. We follow Refs. 33 and 34 and give arguments that the experimentally measured power loss is to a great extent given by the response to a given *external field* [see Eq. (50)]: First, in the contactless measurements the Coulomb fields are weakened when traversing from the meander line to the elec-

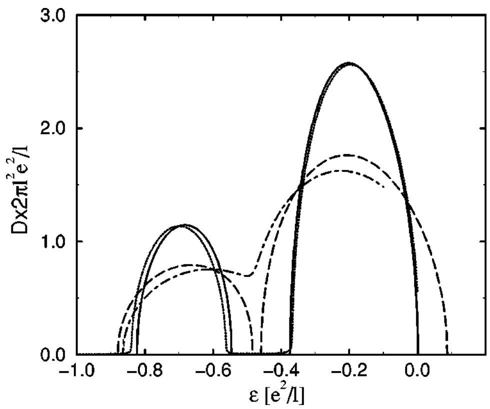

FIG. 3. The thermodynamic density of states at $k_BT=0.03e^2/l$, (solid lines $\Gamma=0.2e^2/l$, dashed lines $\Gamma=0.3e^2/l$, dash-dotted line $\Gamma=0.33e^2/l$) and $k_BT=0.01e^2/l$ (dotted line $\Gamma=0.2e^2/l$).

tron gas. Second, the Coulomb field of the induced charges is coupled to the source of the electromotoric force, the rf generator, only through the meander-line transducer effect. Third, only a small amount of the incident power is absorbed by the electron system. Therefore, the feedback of the induced charges in the two-dimensional electron gas to the power source is strongly reduced. The electron system thus basically reacts to an externally given potential rather than to an effective potential and p^{ext} is measured according to Eq. (50).

The oscillator strength f_{n0} of the nth excitation is defined as[31]

$$\begin{aligned} f_{n0} &= \int_{\epsilon_{n0}-\delta}^{\epsilon_{n0}+\delta} d\omega\, p(\vec{q},\omega) \\ &= -\frac{1}{4\pi q}\int_{\epsilon_{n0}-\delta}^{\epsilon_{n0}+\delta} d\omega\,\omega\,\mathrm{Im}[\epsilon^{-1}_{0,0}(q,\omega)] \\ &= -\frac{e^2}{2q^2}\int_{\epsilon_{n0}-\delta}^{\epsilon_{n0}+\delta} d\omega\,\omega\,\mathrm{Im}[\hat{\chi}_{0,0}(\vec{q},\omega)], \end{aligned} \tag{53}$$

where ϵ_{n0} is the energy of the nth excitation and δ defines a small surrounding energy interval containing no other excitation. The oscillator strengths obey the sum rule

$$\sum_n f_{n0}(q) = \pi e^2 n_s/4m. \tag{54}$$

III. RESULTS

A. The ground state

Figure 3 shows for three disorder strengths the thermodynamic density of states of the electron solid calculated in our model. The general structure of these results has been discussed in detail in Ref. 25: In the hexagonal electron lattice the Coulomb interaction which is taken in mean-field theory creates a periodic effective potential of the same symmetry. If not stated otherwise we assume that there are four magnetic flux quanta per unit cell of the lattice leading to a filling factor of $\nu=1/4$. From general grounds we then expect a splitting of the lowest Landau level into four subbands.[35] At low disorder, in our self-consistent procedure an effective potential results in which the lowest (occupied) subband is separated from the three (unoccupied) upper bands by a pronounced energy gap. The three upper conductionlike bands merge in the disorder potential. In the rest of the paper we mostly consider the electron solid at a temperature of $\beta=0.03e^2/l$. The three curves in Fig. 3 at this temperature represent three special cases. At strong disorder, $\Gamma=0.33e^2/l$, there is a dip in the density of states at the Fermi level together with crystalline order in the sample. In Ref. 26 it was shown that the dc conductivity in this impurity range has an algebraic temperature dependence which is also seen in experiments. At about $\Gamma=0.30e^2/l$ there opens a gap in the density of states that becomes comparable to the thermal energy. In this disorder range there is a turnover to exponentially activated transport. In the cleanest considered system $\Gamma=0.2e^2/l$ the thermal energy is smaller than the width of the gap which can then be regarded as independent of the temperature. This is demonstrated in Fig. 3. As we reduce at $\Gamma=0.2e^2/l$ the temperature to a third, $\beta=0.01e^2/l$ (dotted lines), the curve of the density of states is nearly unchanged and the relative change of the width of the gap is much smaller than a third. The activation energy can thus be regarded as constant.

A reasonable approximation for the effective potential is obtained assuming the strong magnetic-field limit of the electron distribution[27]

$$n(\vec{k}) = \frac{\nu}{2\pi l^2}\exp(-k^2l^2/4). \tag{55}$$

Restricting ourselves to wave vectors in the first shell of the reciprocal lattice (e.g., the three vectors $\vec{k}_1=q_0\vec{u}_y$, $\vec{k}_2=q_0/2(\sqrt{3}\vec{u}_x-\vec{u}_y)$, $\vec{k}_3=\vec{k}_1+\vec{k}_2$ and their negatives, where $q_0=4\pi/(\sqrt{3}a)$ and a is the distance of two neighboring electrons), we obtain for the effective potential

$$\begin{aligned} V(x,y) &= \frac{e^2}{l}\frac{2\nu}{k_1 l}\exp(-k_1^2l^2/4) \\ &\quad\times\left\{\cos(q_0y)+\cos\left[\frac{q_0}{2}(\sqrt{3}x-y)\right]\right\}. \end{aligned} \tag{56}$$

The potential difference V_{mm} between maximum and minimum can be expressed as

$$V_{mm} = \frac{e^2}{l}3.3\sqrt{\nu}\exp(-1.8\nu). \tag{57}$$

The modulation of the effective potential is close to e^2/l with a factor of 1.1 for $\nu=0.25$ and 0.9 for $\nu=0.1$. This consideration explains the energy scale of Fig. 3. For strong magnetic fields above 10 T and a GaAs heterostructure this broadening of the density of states has a typical energy $e^2/(\epsilon l)$ ($\epsilon\approx12.4$) in the order of 10 meV which is in the infrared regime.

Figure 4 demonstrates that a sequence of low-disorder phase → strong-disorder phase → disappearance of hexagonal order may not only result when going from low to strong disorder but also from strong to weak magnetic field. In the upper part of this figure we plot the order parameter $\rho(\vec{k}_1)$ [see Eqs. (11) and (15)] versus the filling factor. For small

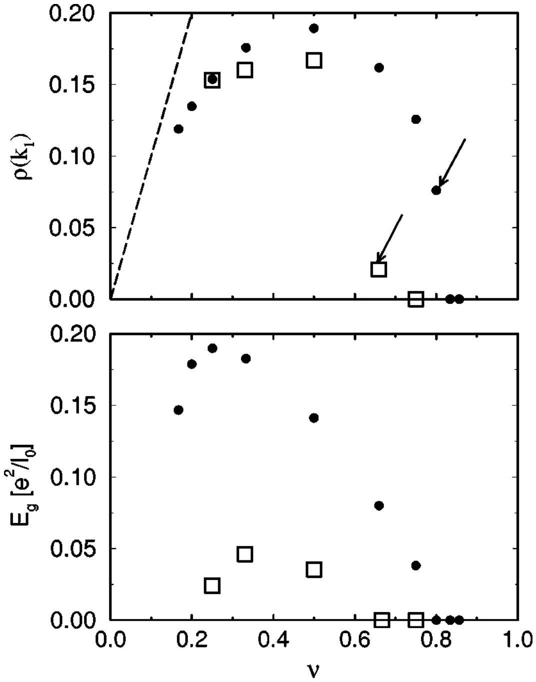

FIG. 4. Upper part: Order parameter $\rho(\vec{k}_1)$ vs filling factor at $\beta=0.03e^2/l$, solid circles $\Gamma=0.2e^2/l$ and open squares $\Gamma=0.3e^2/l$. The dashed line is the strong magnetic-field limit of Eq. (55). Lower part: Width of the energy gap vs filling factor in units of e^2/l_0 where l_0 is the magnetic length at $\nu=1/4$. The arrows mark the points in which the strong-disorder phase is stable.

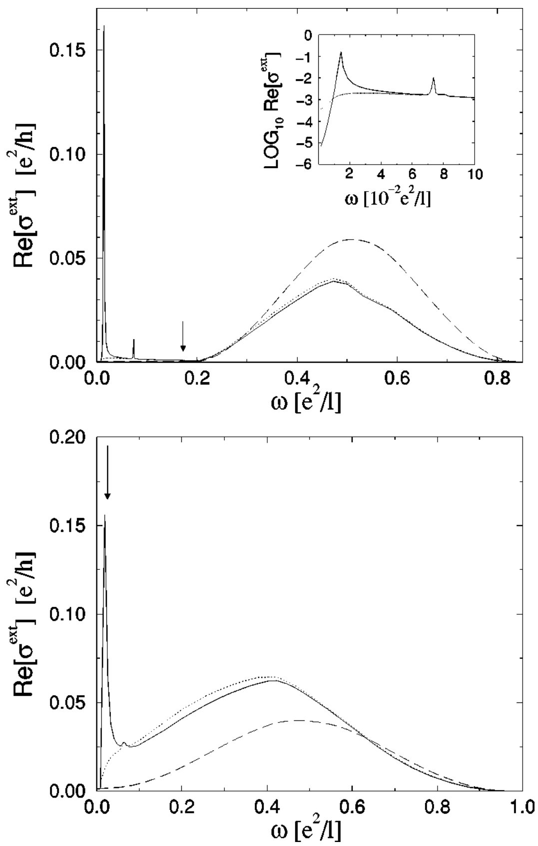

FIG. 5. Real part of the conductivity vs frequency for $\Gamma=0.3e^2/l$, (lower part) and $\Gamma=0.2e^2/l$ (upper part). In solid lines is shown the response to the external electric field and in dotted lines is shown the response to the effective field. $\vec{q}$ is in direction of the X point at the edge of the first Brillouin zone as defined in Ref. 26 with $q/(2X)=0.2$. The temperature is given by $\beta=0.03e^2/l$, the vertical arrows mark the position of the energy gap. The dashed line denotes the combined density of states (relative units).

filling factors the order parameter is close to the value ν. This behavior is expected from the strong magnetic-field limit in Eq. (55). At about $\nu=0.4$ there is a turnover to decreasing order parameter with further increasing filling factor. Finally, the order parameter becomes zero at $\Gamma=0.2e^2/l$ for $\nu=5/6=0.834$ and at $\Gamma=0.3e^2/l$ for $\nu=3/4$. From Fig. 4(b) it can be found that the width of the energy gap roughly follows the same ν dependence. However, the energy gap vanishes already for $\Gamma=0.2e^2/l$ at $\nu=2/3$ and for $\Gamma=0.3e^2/l$ at $\nu=4/5$. Around $\nu=2/3$ for $\Gamma=0.2e^2/l$ and $\nu=4/5$ and for $\Gamma=0.3e^2/l$ the strong-disorder phase is the ground state. The density of states then only has a dip at the Fermi level and looks qualitatively like the result for $\Gamma=0.33e^2/l$ in Fig. 3.

B. Low-energy excitation spectrum

Figure 5 shows the diagonal element $(\vec{k}=\vec{k}'=0)$ of the real part of the longitudinal conductivity σ^{ext} in response to the external electric field [Eq. (52)]. According to Eq. (50) the real part of σ^{ext} gives up to a factor of 2 the power absorbed by the the electron system per unity of the external field. Following standard linear-response theory the poles of ϵ^{-1} and therefore the poles of σ^{ext} yield the longitudinal excitation frequencies of the electron solid.[36]

In the curves of Fig. 5 we can distinguish two frequency domains which are separated by the frequency of the energy gap which is marked by a vertical arrow: In the regime of smaller frequencies there are discrete excitation peaks on top of a background of a small, thermally activated response. These peaks will be considered in detail in context with the following figures. For energies above the energy gap there is a broad frequency domain with increased conductivity. A comparison with the combined density of states shows that this frequency domain is defined through the range of possible single-particle excitations from the occupied valence-type band to the empty conduction-type energy bands. A reasonable estimate for the position of the maximum of the single-particle excitations is half the potential V_{mm} as defined in Eq. (57), which for the relevant magnetic fields stronger than 10 T puts this frequency range into the infrared regime, a few times less than the cyclotron resonance. As expected, the position and the weight of the single-particle resonance is nearly independent of the wave vector. Its weight decreases with lesser disorder.

We also depict in Fig. 5 the real part of the conductivity σ in response to the effective field as defined in Eq. (51). As a general result the curve of σ^{ext} follows that of σ very closely at higher frequencies. The deviations for lower frequencies are plotted in the inset of Fig. 5(a): First, the lowest excitation which will later be shown to be the magnetophonon pole vanishes completely for σ, and second for even smaller frequencies σ drops much slower than σ^{ext}. Both these properties are important in the limit $\vec{q},\omega\rightarrow 0$ that determines the dc conductivity. The disappearance of the magnetophonon peak

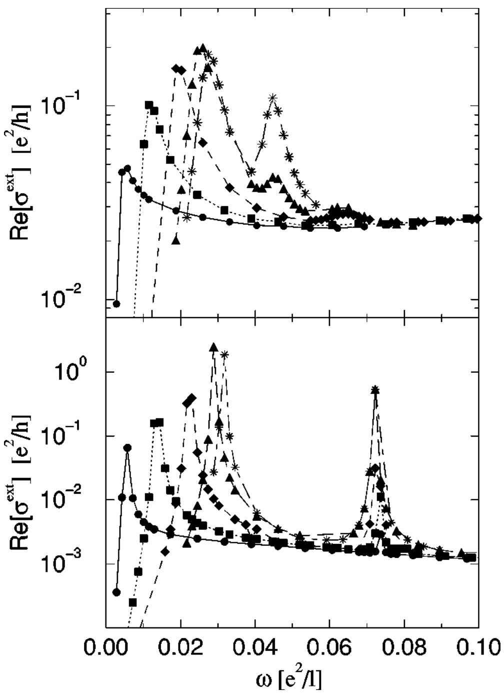

FIG. 6. Real part of the conductivity upper figure for $\Gamma = 0.3e^2/l$, lower part for $\Gamma = 0.2e^2/l$. Temperature and direction of $\vec{q}$ are as in Fig. 5 with $q/(2X) = 0.1$ (circles), 0.2 (squares), 0.3 (diamonds), 0.4 (triangles), and 0.5 (stars).

in σ also results in the harmonic approximation[37] and is caused by the long-range part of the Coulomb interaction.

Figure 6 shows the real part of σ^{ext} for small frequencies at various wave vectors. At both impurity strengths two low-lying excitations can be observed. At $\Gamma = 0.3e^2/l$ there is a bump between $\omega = 0.06e^2/l$ and $0.07e^2/l$ that can be interpreted as a third one. The lowest excitation shows a strong q dependence in contrast to the second excitation with a flat dispersion. The second resonance grows continually with larger wave vectors up to the edge of the first Brillouin zone where $q/(2X) = 0.5$, the lowest excitation has a maximum peak height at $q/(2X) = 0.4$. For finite frequencies the curves seem to approach a weak, close-to linear dependence of $\ln[\mathrm{Re}(\sigma^{\mathrm{ext}})]$ on ω.

Figure 7 shows the dispersion of the two lowest excitations. The higher excitation shows no dependence on the wave vector. We therefore interpret it as a local oscillation basically at a single site of the Wigner crystal with weak coupling to neighboring sites. Its frequency is considerably lowered with increasing disorder. The curves are discontinued for smaller wave vectors when this ''local mode'' becomes so weak that it cannot be resolved any more. In dot-dashed lines the $q^{2/3}$ dispersion of the magnetophonon in the harmonic approximation[38] is plotted. Since in this long-wavelength approximation the off-diagonal elements of the susceptibility are neglected no gap opens at the edge of the Brillouin zone. We compare our quantum results for the lowest mode with the dispersion in the harmonic approximation. In the central region of the first Brillouin zone, for $0.1 \leqslant q/(2X) \leqslant 0.3$, the quantum-mechanical results approach the classical dispersion for decreasing disorder. In calculations for zero disorder such a coincidence has already been found in Ref. 27. We therefore interpret the lowest excitation as magnetophonon mode in the disordered electron gas. Our microscopic calculations show that in the disordered system the dispersion for small wave vectors approaches a constant instead of the $q^{2/3}$ law. This constant increases with increasing disorder. In the case of $\Gamma = 0.3e^2/l$ which is close to the maximum disorder in which the solid phase is still stable we read off a value for the $q \to 0$ limit given by $\Omega \approx \alpha e^2/l$ with $\alpha = 0.004$. If we assume a typical experimental magnetic field of 12 T and introduce the dielectric constant of GaAs, $\epsilon = 12.4$ we end up with an energy of $\Omega = 0.06$ meV corresponding to a frequency of 14 GHz. For the cleaner system we read off $\alpha = 0.0028$ corresponding to a frequency of 10 GHz. The excitation frequencies measured in experiments at these magnetic fields are smaller, ranging between one and two GHz (Refs. 32, 6, 18, and 16). In view of the strong approximations that have to be introduced to make possible a consistent response theory of the disordered electron solid no better agreement can be expected. Among others we see three major sources to explain the discrepancy between theory and experiment: First, our mean-field theory that leads to a long-range hexagonal order is too simple, second, the SCBA approximation for the impurity interaction is insufficient for quantitative predictions and third, the experimental systems might be less disordered than assumed in our calculations.

We compare our results for the magnetophonon in the disordered electron solid with a theory in which the Coulomb interaction is also taken in the Hartree-Fock approximation but the disorder potential is represented by an external washboard potential that is commensurate with the electron solid.[38] In the latter case the dispersion has a linear leading-order term in q, i.e., for small q it can be written as $\omega(q) \approx \Omega + \beta q$.[39] In our microscopic theory with strong disorder the dispersion is much softer equivalent to $\omega(q) \approx \Omega + \beta q^n$, $n \geqslant 2$.

In the experiments of Refs. 18 and 16 a resonance in the GHz regime was observed and studied with changing magnetic field: Starting from a well-developed resonance peak at strong magnetic fields the resonance broadens at weaker magnetic fields. The peak height and the frequency of the maximum decrease. For weaker magnetic fields but still in the insulating regime the peak vanishes in an enhanced background conductivity. Based on our numerical analysis we

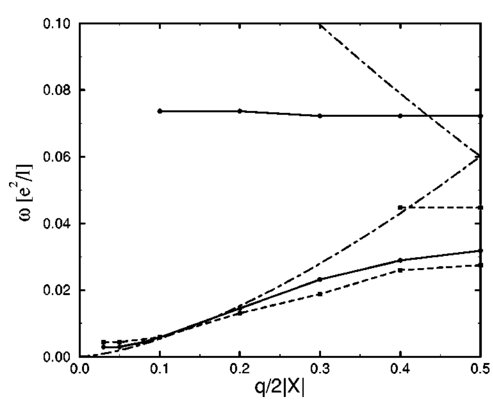

FIG. 7. Dispersion of the two lowest excitations for $\Gamma = 0.30e^2/l$ (dashed lines), $\Gamma = 0.2$ (solid lines). The dot-dashed line shows the result of the harmonic approximation in the long-wavelength limit.

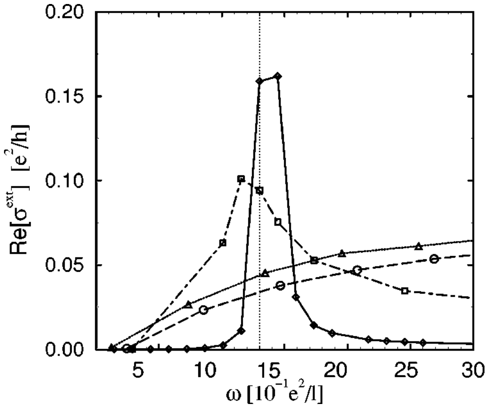

FIG. 8. Real part of σ^{ext} vs frequency at $q/(2X)=0.2$ for $\Gamma=0.20e^2/l$ (solid line), $\Gamma=0.3$ (dash-dotted line) and $\Gamma=0.33e^2/l$ (dashed line) and at $q/(2X)=0.1$ for $\Gamma=0.33e^2/l$ (dotted line). The other parameters are like in Fig. 5.

associate with the experimental resonance the magnetophonon in the disordered electron crystal and offer a Landau damping picture as an explanation for the changes with varying magnetic field. Our picture is demonstrated in Fig. 8: In the experiments,[3,5] it has been reported that the activation energy of the dc transport is an increasing function of the magnetic field. In agreement with these experimental findings we can associate the activation energy with the energy gap between valence band and conduction band (see Fig. 4). For large magnetic fields, therefore, a situation results as for $\Gamma=0.2e^2/l$ (Fig. 5 and solid line in Fig. 8). The magnetophonon frequency at the small experimental q vectors is located deep in the energy gap. We find at the smallest considered wave vector in Fig. 5 that the height of the magnetophon peak is decreased but that there is still a factor of more than 10 between the conductivity background and the peak conductivity. For weaker magnetic fields the size of the energy gap is reduced and the situation becomes like in Fig. 5(a) ($\Gamma=0.3e^2/l$): The magnetophonon frequency becomes larger than or comparable to the width of the energy gap. In this case the magnetophonon can couple to single-particle excitations and Landau damping can occur. As is typical for Landau damping, Fig. 8 shows that the width of the magnetophonon peak increases and that the peak conductivity decreases. The reduction of the excitation frequency with lower magnetic fields can be seen as a typical phenomenon of Landau damping, which for example, also occurs in plasmon excitations in alkali metals and can be found in Fig. 8 comparing the results for $\Gamma=0.2e^2/l$ and $\Gamma=0.3e^2/l$. For still smaller magnetic field the energy gap vanishes and only a dip in the density of states is present. This is the case for $\Gamma=0.33$. Because of this reduced density of states we still expect an increased resistance of the electron gas. Figure 8 shows that like in the experiments the magnetophonon resonance vanishes in this regime. In Ref. 40 elastic theory was applied to the Wigner crystal in the weak-pinning limit. It was shown that in this case also a pinning mode can result with frequencies increasing with the magnetic field. However, in contrast with the experiments the width of the peak is a decreasing and the height of the peak is a growing function of the magnetic field. Though our theory gets the experimentally observed qualitative features right, we emphasize that we can only recover qualitative features of the experiments in our model. Because of the strong approximations made in our theory there is no quantitative agreement.

IV. SUMMARY

In conclusion we present a quantum formalism to calculate consistently response properties of the disordered Wigner crystal in strong magnetic fields. We find two phases with distinct properties, a crystalline low-disorder phase with a pronounced energy gap and an ''amorphous'' strong-disorder phase with a finite density of states at the Fermi level. The transition from a low- to a strong-disorder phase can be driven by a decrease in the applied magnetic field: In the crystalline regime the magnetophonon frequency of the disordered system lies well in the energy gap and the excitation peak is sharp. At the transition to the strong-disorder phase the frequency of the collective mode enters the regime of possible single-particle transitions. The mode shows typical Landau damping: It is broadened and its frequency decreases slightly. Finally, when the strong-disorder phase becomes stable, the excitation becomes overdamped. In this picture we explain recent experimental results by Li *et al.*[18] and Engel *et al.*[16]

APPENDIX A: EVALUATION OF THE BUBBLE WITH A SINGLE IMPURITY INTERACTION LINE

We insert the Fourier transform of the impurity interaction line Eq. (29) and the representation of the Green's function given in Eq. (3) in Eq. (28) and obtain

$$\hat{\Pi}^{1}_{\vec{k},\vec{k}'}(\vec{q},i\omega_n)$$
$$=\frac{1}{\beta}\sum_{n',\vec{p}}\frac{w(\vec{p})}{S}\sum_{X_1,\vec{k}_1,X_1',\vec{k}_1',X_2,\vec{k}_2,X_2',\vec{k}_2'}G(\vec{k}_1,i\omega_{n'}+i\omega_n)$$
$$\times G(\vec{k}_1',i\omega_{n'}+i\omega_n)G(\vec{k}_2,i\omega_n)G(\vec{k}_2',i\omega_n)$$
$$\times\exp[ik_{1x}X_1+ik_{1x}'X_1'+ik_{2x}X_2+ik_{2x}'X_2']$$
$$\times\exp[-l^2/2(k_{1x}k_{1y}+k_{1x}'k_{1y}'+k_{2x}k_{2y}+k_{2x}'k_{2y}')]$$
$$\times\langle X_2'-k_{2y}'l^2|\exp(-i\vec{p}\vec{r})|X_2\rangle\langle X_1-k_{1y}l^2|$$
$$\times\exp(i\vec{p}\vec{r})|X_1'\rangle\langle X_2-k_{2y}l^2|\exp[-i(\vec{q}+\vec{k})]|X_1\rangle$$
$$\times\langle X_1'-k_{1y}'l^2|\exp[i(\vec{q}+\vec{k}')]|X_2'\rangle. \quad \text{(A1)}$$

Further inserting the matrix elements of Eq. (24) yields

$$\hat{\Pi}^{1}_{\vec{k},\vec{k}'}(\vec{q},i\omega_n)$$
$$=\frac{\hat{A}_{\vec{k},\vec{k}'}(\vec{q})}{\beta}\sum_{i\omega_n'}\sum_{\vec{k}_1,\vec{k}_2}G(\vec{k}_1,i\omega_{n'}+i\omega_n)G(\vec{k}_2,i\omega_n)$$
$$\times\exp\left\{i\frac{l^2}{2}[(\vec{k}_2\times\vec{k}_1)+(\vec{k}_1-\vec{k}_2)(\vec{q}+\vec{k})]_z\right\}$$
$$\times\sum_{\vec{p}}\frac{w(\vec{p})}{S}\exp\{il^2[(\vec{k}_1+\vec{k}_2-\vec{q}-\vec{k})\times\vec{p}\,']\}$$

$$\times\exp\left(-\frac{p^2l^2}{2}\right)\sum_{\vec{k}_1',\vec{k}_2'}\delta(\vec{k}_1+\vec{k}_2-\vec{k},-\vec{k}_1'-\vec{k}_2-\vec{k}')$$

$$\times G(\vec{k}_1',i\omega_{n'}+i\omega_n)G(\vec{k}_2',i\omega_n)\exp\left\{i\frac{l^2}{2}[(\vec{k}_1'\times\vec{k}_2')\right.$$

$$\left.+(\vec{k}_1'-\vec{k}_2')\times(\vec{q}+\vec{k}')]_z\right\}. \quad \text{(A2)}$$

We now define

$$\vec{P}=\vec{k}_1+\vec{k}_2-\vec{k}-\vec{q}=-\vec{k}_1'-\vec{k}_2'-\vec{k}-\vec{q} \quad \text{(A3)}$$

to eliminate $\vec{k}_2$ and $\vec{k}_2'$ and find

$$\hat{\Pi}^1_{\vec{k},\vec{k}'}(\vec{q},i\omega_n)=\frac{\hat{A}_{\vec{k},\vec{k}'}(\vec{q})}{\beta}\sum_{i\omega_n',\vec{P}}\sum_{\vec{k}_1}G(\vec{k}_1,i\omega_{n'}+i\omega_n)$$

$$\times G(\vec{P}-\vec{k}_1+\vec{k}+\vec{q},i\omega_n)$$

$$\times\exp\left[i\frac{l^2}{2}(\vec{P}-\vec{q}-\vec{k})\times\vec{k}_1\right]$$

$$\times\exp\left\{i\frac{l^2}{2}[\vec{P}\times(\vec{k}'-\vec{k})]\right\}$$

$$\times\sum_{\vec{p}}\frac{w(\vec{p})}{S}\exp[il^2(\vec{P}\times\vec{p})]$$

$$\times\exp\left(-\frac{p^2l^2}{2}\right)\sum_{\vec{k}_1'}G(\vec{k}_1',i\omega_{n'}+i\omega_n)$$

$$\times G(-\vec{P}-\vec{k}_1'-\vec{k}'-\vec{q})$$

$$\times\exp\left[i\frac{l^2}{2}(\vec{P}-\vec{q}-\vec{k}')\times\vec{k}_1'\right]. \quad \text{(A4)}$$

Equations (32) and (35) follow after the substitutions $\vec{P}\to -\vec{K}-\vec{q}$, $\vec{k}_1\to\vec{k}_1+\vec{k}$ and $\vec{k}_1'\to\vec{k}_1'+\vec{K}$.

APPENDIX B: SUMMATION OVER THE MATSUBARA FREQUENCIES

In this appendix we want to demonstrate how the Matsubara frequency summation in Eq. (38) can be done using standard techniques described in Ref. 28. A similar problem has been solved in Ref. 29. In the first step we use the residue theorem to write

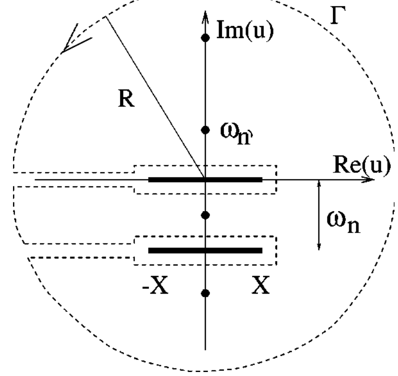

FIG. 9. Path of integration.

$$\hat{\Pi}_{\vec{k},\vec{k}'}(\vec{q},i\omega_n)=-\hat{A}_{\vec{k},\vec{k}'}\int_\Gamma\frac{du}{2\pi i}n_F(u)\hat{\pi}_{\vec{k},\vec{k}'}(\vec{q},i\omega_n,u). \quad \text{(B1)}$$

Here $n_F(u)=[\exp(\beta z)+1]^{-1}$ is the Fermi distribution function which has poles with residues $-1/\beta$ at the fermionic Matsubara frequencies. For the integration a contour Γ is chosen as depicted in Fig. 9. Apart from the poles introduced through the Fermi distribution function the integrand is regular in the area enclosed by Γ. To achieve this the two cuts at $\mathrm{Im}(u)=0$ and $\mathrm{Im}(u)=-\omega_n$ are taken out. At these cuts there is a discontinuity of $\hat{\pi}^0$ in the interval $-X\leqslant\mathrm{Re}(u)\leqslant X$ which is caused by the imaginary parts of the Green's-function factors entering in $\hat{\pi}^0$ according to Eq. (25). The interval $[-X,X]$ is the energy range with a nonvanishing density of states. It is obtained from the ground-state calculations and found to be well defined. Outside the interval $[-X,X]$ the integrand of Eq. (B1) is continuous and no contribution to the contour integral results from the cuts at $\mathrm{Im}(u)=0$ and $\mathrm{Im}(u)=-\omega_n$. In the limit $R\to\infty$ the contribution of the circular part of Γ vanishes and we find

$$\hat{\Pi}_{\vec{k},\vec{k}'}(\vec{q},i\omega_n)$$

$$=-\hat{A}_{\vec{k},\vec{k}'}\int_{-X}^{X}\frac{d\epsilon'}{2\pi i}n_F(\epsilon')\{\hat{\pi}_{\vec{k},\vec{k}'}(\vec{q},i\omega_n,\epsilon'+i\delta)$$

$$-\hat{\pi}_{\vec{k},\vec{k}'}(\vec{q},i\omega_n,\epsilon'-i\delta)+\hat{\pi}_{\vec{k},\vec{k}'}[\vec{q},i\omega_n,\epsilon'+i(-\omega_n+\delta)]$$

$$-\hat{\pi}_{\vec{k},\vec{k}'}[\vec{q},i\omega_n,\epsilon'-i(\omega_n+\delta)]\},$$

where ϵ' is a real energy variable and we have used the periodicity of the Fermi function $n_F(u+i\omega_n)=n_F(u)$. In the next step we introduce the analytic continuation $i\omega_n\to v$ and find for real $v=\epsilon$ the expression Eq. (39).

[1] E. P. Wigner, Phys. Rev. **46**, 1002 (1934).
[2] V. M. Pudalov, M. D'Iorio, S. V. Krachenko, and J. W. Campbell, Phys. Rev. Lett. **70**, 1866 (1993); J. Yoon, C. C. Li, D. Shahar, D. C. Tsui, and M. Shayegan, cond-mat/9807235 (unpublished).
[3] R. L. Willett, H. L. Stormer, D. C. Tsui, L. N. Pfeiffer, K. W. West, and K. W. Baldwin, Phys. Rev. B **38**, 7881 (1988).
[4] H. W. Jiang, R. L. Willett, H. L. Stormer, D. C. Tsui, L. N. Pfeiffer, and K. W. West, Phys. Rev. Lett. **65**, 633 (1990).
[5] V. J. Goldman, M. Santos, M. Shayegan, and J. E. Cunningham, Phys. Rev. Lett. **65**, 2189 (1990).
[6] M. A. Paalanen, R. L. Willett, P. B. Littlewood, R. R. Ruel, K. W. West, L. N. Pfeiffer, and D. J. Bishop, Phys. Rev. B **45**, 11 342 (1992); M. A. Paalaneni, R. L. Willet, R. R. Ruel, P. B. Littlewood, K. W. West, and L. N. Pfeiffer, *ibid.* **45**, 13 784 (1992).

[7] M. B. Santos, Y. W. Suen, M. Shayegan, Y. P. Li, L. W. Engel, and D. C. Tsui, Phys. Rev. Lett. **68**, 1188 (1992); M. B. Santos, J. Jo, Y. W. Suen, L. W. Engel, and M. Shayegan, Phys. Rev. B **46**, 13 639 (1992).
[8] H. C. Manoharan and M. Shayegan, Phys. Rev. B **50**, 17 662 (1994).
[9] P. K. Lam and S. M. Girvin, Phys. Rev. B **30**, 473 (1984); D. Levesque, J. J. Weis, and A. H. MacDonald, *ibid.* **30**, 1056 (1984); H. Y. Yi and H. A. Fertig, *ibid.* **58**, 4019 (1998).
[10] X. Zhu and S. G. Louie, Phys. Rev. Lett. **70**, 335 (1993); R. Price, P. M. Platzman, and S. He, *ibid.* **70**, 339 (1993).
[11] R. L. Willett, H. L. Stormer, D. C. Tsui, L. N. Pfeiffer, K. W. West, M. Shayegan, M. Santos, and T. Sajoto, Phys. Rev. B **40**, 6432 (1989).
[12] Y. P. Li, T. Sajoto, L. W. Engel, D. C. Tsui, and M. Shayegan, Phys. Rev. Lett. **67**, 1630 (1991).
[13] E. Y. Andrei, G. Deville, D. C. Glattli, F. I. B. Williams, E. Paris, and B. Etienne, Phys. Rev. Lett. **60**, 2765 (1988).
[14] H. L. Stormer and R. L. Willett, Phys. Rev. Lett. **62**, 972 (1989).
[15] D. Shahar, D. C. Tsui, M. Shayegan, R. N. Bhatt, and J. E. Cunningham, Phys. Rev. Lett. **74**, 4511 (1995); M. Shayegan, Solid State Commun. **102**, 155 (1997).
[16] L. W. Engel, C.-C. Li, D. Shahar, D. C. Tsui, and M. Shayegan, Solid State Commun. **104**, 167 (1997).
[17] V. T. Dolgopolov, G. V. Kravchenko, A. A. Shashkin, and S. V. Kravchenko, Phys. Rev. B **46**, 13 303 (1992); S. V. Kravchenko, J. A. A. J. Perenboom, and V. Mi. Pudalov, *ibid.* **44**, 13 513 (1991).
[18] C.-C. Li, L. W. Engel, D. Shahar, D. C. Tsui, and M. Shayegan, Phys. Rev. Lett. **79**, 1353 (1997).
[19] S. Kivelson, D.-H. Lee, and S.-C. Zhang, Phys. Rev. B **46**, 2223 (1992).
[20] H. Aoki, J. Phys. C **12**, 633 (1979).
[21] S. T. Chui and B. Tanatar, Phys. Rev. Lett. **74**, 458 (1995).
[22] T. Ando and Y. Uemura, J. Phys. Soc. Jpn. **36**, 959 (1974); T. Ando, A. B. Fowler, and F. Stern, Rev. Mod. Phys. **54**, 437 (1982).
[23] G. Baym and L. P. Kadanoff, Phys. Rev. **124**, 287 (1961).
[24] U. Wulf, J. Kučera, and E. Sigmund, Phys. Rev. Lett. **77**, 2993 (1996).
[25] U. Wulf and A.H. MacDonald, Phys. Rev. B **47**, 6566 (1993).
[26] U. Wulf, Phys. Rev. B **52**, 12 120 (1995).
[27] R. Côté and A. H. MacDonald, Phys. Rev. B **44**, 8759 (1991); Phys. Rev. Lett. **65**, 2662 (1990).
[28] G. D. Mahan, *Many-Particle Physics* (Plenum, New York, 1986), Chap. 3.3.
[29] D. Antoniou, A. H. MacDonald, and J. Swihart, Phys. Rev. B **41**, 5440 (1990).
[30] J. D. Jackson, *Classical Electrodynamics* (Wiley, New York, 1975), Chaps. 6.8 and 6.10.
[31] C. Dahl, Phys. Rev. B **41**, 5763 (1990).
[32] G. Deville, A. Valdes, E. Y. Andrei, and F. I. B. Williams, Phys. Rev. Lett. **53**, 588 (1984).
[33] D. C. Glattli, G. Deville, V. Duburcq, and F. I. B. Williams, Surf. Sci. **229**, 344 (1990).
[34] B. G. A. Normand, P. A. Littlewood, and A. J. Millis, Phys. Rev. B **46**, 3920 (1992).
[35] D. R. Hofstadter, Phys. Rev. B **14**, 2239 (1976); A. H. MacDonald, *ibid.* **28**, 6713 (1983).
[36] D. Pines, *Elementary Excitations in Solids* (Benjamin/Cummings, Reading, MA, 1963), Chaps. 3-4.
[37] U. Wulf (unpublished).
[38] R. Côté and A. H. MacDonald, Surf. Sci. **263**, 187 (1992).
[39] H. A. Fertig, Phys. Rev. B **59**, 2120 (1999).
[40] R. Chitra, T. Giamarchi, and P. Le Doussal, Phys. Rev. Lett. **80**, 3827 (1998).